Published in final edited form as:
IEEE J Sel Top Quantum Electron. 2009 October 6; 16(3): 671–697. doi:10.1109/JSTQE.2009.2029547.

Dynamics of Magnetic Nanoparticle-Based Contrast Agents in Tissues Tracked Using Magnetomotive Optical Coherence Tomography

Renu John,
Biophotonics Imaging Laboratory, Beckman Institute for Advanced Science and Technology, University of Illinois at Urbana-Champaign, Urbana, IL 61801 USA

Eric J. Chaney, and
Biophotonics Imaging Laboratory, Beckman Institute for Advanced Science and Technology, University of Illinois at Urbana-Champaign, Urbana, IL 61801 USA

Stephen A. Boppart [Senior Member, IEEE]
Biophotonics Imaging Laboratory, Beckman Institute for Advanced Science and Technology, and the Departments of Electrical and Computer Engineering, Bioengineering, and Medicine, University of Illinois Urbana-Champaign, Urbana, IL 61801 USA

Renu John: renujohn@illinois.edu; Eric J. Chaney: echaney@illinois.edu; Stephen A. Boppart: boppart@illinois.edu

Abstract

Magnetomotive optical coherence tomography (MM-OCT) is an important tool for the visualization and quantitative assessment of magnetic nanoparticles in tissues. In this study, we demonstrate the use of MM-OCT for quantitative measurement of magnetic iron oxide nanoparticle transport and concentration in *ex vivo* muscle, lung, and liver tissues. The effect of temperature on the dynamics of these nanoparticles is also analyzed. We observe that the rate of transport of nanoparticles in tissues is directly related to the elasticity of tissues, and describe how the origin of the MM-OCT signal is associated with nanoparticle binding. These results improve our understanding of how iron oxide nanoparticles behave dynamically in biological tissues, which has direct implications for medical and biological applications of targeted nanoparticles for contrast enhancement and therapy.

Index Terms

Iron oxide; magnetic nanoparticles (MNPs); magnetomotive; optical coherence tomography (OCT)

I. Introduction

Metallic nanoparticles have recently been demonstrated as combined targeting, diagnostic, and therapeutic agents in cancer treatment [1]–[7]. Various researches have demonstrated

Color versions of one or more of the figures in this paper are available online at http://ieeexplore.ieee.org.

the use of magnetic nanoparticles (MNPs) as contrast agents in various imaging modalities such as MRI [8]–[10] and optical coherence tomography (OCT) [11]–[13]. Efforts to design protocols for an effective *in vivo* therapeutic outcome rely on the knowledge of the nanoparticle localization, concentration, and transport through various tissue structures. Efficient transport of nanoparticles into tumor sites remains a critical issue in the application of nanoparticles for various therapeutic and diagnostic applications. A high-resolution noninvasive *in vivo* method to determine interstitial transport and concentration of nanoparticles does not currently exist. In recent years, optical methods have widely been explored as noninvasive tools for diagnostic applications for various disease conditions. Among these, OCT is one of the leading modalities for *in vivo* studies. OCT reveals tissue microstructure up to a few millimeters deep into biological tissues, and generates images based on the optical scattering properties of the cells and tissue.

A model of nanoparticle transport in tissues would be useful for providing more insight into various factors that affect the distribution of nanoparticles in nonvascular regions of tissue, as well as for providing information into the design of efficient drug delivery vehicles. There has been intensive research during the past few decades in the use of nanoscale particles (100 nm or less) in medicine, especially for delivering chemotherapeutic agents to cancer cells [14], [15]. Nanoscale devices carrying chemotherapeutic drugs could extravasate from blood vessels, diffuse through the tissue, and target and enter tumor cells. Drug delivery via nanoparticles offers significant advantages over traditional delivery via systemic bolus injection. Graf and Wittrup [15] have carried out a theoretical analysis of antibody penetration in tumor spheroids based on a diffusion model accounting for various factors like binding, degradation, and plasma clearance. Goodman *et al.* [14] have proposed a mathematical model for drift–diffusion of nanoparticles in a 3-D multicellular tumor spheroid structure and attempted to analyze various factors that influence the nanoparticle penetration. Furlani and Ng [16], [17] have developed an analytical model of magnetic nanoparticle transport through blood and their capture in microvasculatures where they use an external magnetic field to transport the nanoparticles.

OCT is a 3-D microstructural biomedical imaging modality that utilizes the coherence property of light to optically range light scattering structures [10]–[13], [18], [19]. Various types of contrast agents have been developed for OCT that may enhance its biomedical utility by enabling molecular imaging [10], [18]–[21]. Magnetomotive OCT (MM-OCT) is accomplished using an electromagnet that modulates a magnetic field within the tissue during OCT imaging [22]–[26]. This provides a mechanical displacement at the locations of MNPs in the tissue, which is observed as a shift in the OCT interferogram. MM-OCT was first demonstrated in a 3-D-engineered tissue scaffold containing a mixture of microparticle-labeled and microparticle-unlabeled macrophage cells [23]. Using MM-OCT, imaging of MNPs in the digestive tract of an *in vivo* African frog tadpole was demonstrated [24]. The main drawback of this early system was the three-step acquisition process of acquiring two successive axial scans with the magnetic field OFF and a third with the field ON. This was necessary for the rejection of physiological motion for *in vivo* imaging, comparing the signal changes between the ON and OFF scans (magnetomotion) with those between the two OFF

scans (physiological motion). Also, this method only tracked the amplitude of the OCT interference signal.

Recently, an MM-OCT system using a spectral-domain OCT configuration that provides sufficient phase sensitivity for phase-resolved imaging has been demonstrated [25]. In this system, the magnetic gradient force is modulated sinusoidally during a B-mode image frame, and background rejection is accomplished by acquiring an *a priori* image frame with the magnetic field OFF. In this paper, we demonstrate the biological application of this technology in studying the dynamics of MNPs in biological tissues. We demonstrate the use of MM-OCT for quantitative measurements of MNP transport and concentration in *ex vivo* tissues.

II. Principles of Magnetomotion in Biological Tissues

In this section, we will first describe the basic concept of magnetomotion of MNPs in biological media, and how it is effectively exploited in an OCT system to obtain useful information about the media, as well as the nanoprobes. A short explanation of how OCT is used to detect magnetomotion, and how the data is collected and processed to produce images with magnetomotive contrast follows. A detailed theory and a theoretical model of the system assuming a homogeneous distribution of MNPs in the tissues is presented in earlier papers [23]–[25] published by our group.

A spectral-domain OCT system is used for the experiments to extract the magnetomotive signal from the sample. In our MM-OCT system, the magnetic field is applied using a solenoid, and imaging is performed on the sample immediately below the solenoid bore. Within the imaging volume of the sample, the radial components of the magnetic field are negligible and the magnetic field gradient is predominantly in the axial direction. In contrast to other solenoid geometries [23], use of an air-core solenoid with a central bore allows the OCT sample arm to be focused onto the sample through the central bore, thus allowing *in vivo* imaging and imaging of thick tissues.

We perform 2-D B-mode imaging of the sample twice, once with the field OFF and once with the field ON. 2-D data is acquired with one axis as the axial (z) depth direction and the other axis as the coupled transverse/temporal dimension. We can couple the mechanical excitation with the B-mode OCT scanning by modulating the magnetic field several cycles during the time taken to mechanically scan the imaging beam spot over one resolution point. It should be noted that the axial line acquisition rate must be sufficiently fast to meet the Nyquist criterion for sampling the modulating magnetic field frequency. Also, the magnetomotive signal must be separated from the optical scattering changes in the x-dimension. These conditions can be met by following:

$$f_z > 2f_B > \frac{2v}{\Delta x} \quad (1)$$

where f_z is the axial (z) line acquisition rate, Δx is the transverse resolution of the OCT system, and v is the velocity of the transverse scan. The latter criterion requires that more than one cycle of the magnetic field be completed in the time it takes to transversely scan

across one point scatterer. By following this method, we are encoding the coupled spatial and temporal channel (*x*-/*t*-dimension) with different frequency bands of the same "image." To reconstruct the MM-OCT image, raw image data is bandpass filtered (BPF) about f_B with a bandwidth of $v/\Delta x$ followed by an inverse Fourier transformation.

A 2-D Fourier transform of the spectral interference pattern after background subtraction of the reference field intensity would give the 2-D B-mode image. This complex analytical signal can be expressed in the form

$$\begin{aligned}\tilde{S}(x,z;t) &= S_{\text{env}}(x,z;t)\exp(i\phi(x,z;t)) \\ &\approx S_{\text{env}}(x,z)\exp(i\phi(x,z))\exp(2ik\Delta z(x,z;t)), \quad \text{for } \Delta z \ll l_c.\end{aligned} \tag{2}$$

where $S_{\text{env}}(x, z)$ and $\varphi(x, z)$ indicate the B-mode image in the absence of magnetomotion. When the displacement Δz is small compared to the coherence length l_c, S_{env} is unchanged and Δz only affects the phase term. The second phase term is caused by the displacement of the sample in the elastic regime, due to the magnetomotive force. This can be expressed as

$$\Delta z(t) = A\left(\frac{\sin(2\pi f_B t+\varphi)+1}{2}\right). \tag{3}$$

where the magnetic field is sinusoidally modulated in time, A is the maximum amplitude of the displacement, and ϕ is the mechanical phase lag. If the viscosity of the medium can be ignored, the value of ϕ will equal zero for a paramagnetic system (aligned motion) and π for a diamagnetic system (opposed motion). However, even in media with significant viscosity, one would expect to observe a shift of π when comparing para-and diamagnetic media. It has been found experimentally that most of the biological tissues are inherently diamagnetic in nature [27] giving a π phase lag. In this way, ϕ can be used to determine the direction of the magnetomotive force.

The magnetomotive terms can be extracted from the B-mode data by computing the complex argument and taking a derivative of (2)

$$\begin{aligned}D(x,z;t) &= \frac{\partial}{\partial t}\left\{\arg\left(\tilde{S}(x,z;t)\right)\right\} \\ &= \frac{\partial}{\partial t}\{2k\Delta z(x,z;t)+\phi(x,z)\} \\ &= 2\pi f_B kA(x,z)\cos(2\pi f_B t+\varphi(x,z))+\frac{\partial}{\partial t}\phi(x,z).\end{aligned} \tag{4}$$

Phase unwrapping is performed to bring the total phase change to within 2π. The derivative contributes by removing unwanted low-frequency noise. The magnetomotive term modulated at f_B can thus be extracted by applying a BPF to the Fourier transform of D along the transverse *x*/coupled temporal dimension about f_B with an appropriate passband to preserve spatial *x* variations. The mechanical phase lag $\varphi(x, z)$ is similarly extracted by computing the argument of the BPF D. From the measured mechanical phase lag ϕ for a position in the tissue $\vec{r}$, a normalized cosine filter $\hat{f}$ that suppresses diamagnetic signals has been employed pointwise to the extracted MM-OCT signal given by

$$\hat{f}(\vec{r}) = \left(\frac{\cos(\varphi(\vec{r})) + 1}{2} \right). \quad (5)$$

Thus, the background-rejected magnetomotive signal $S_{\mathrm{m\,m}}$ in decibels can be written as follows:

$$S_{\mathrm{m\,m}}(x,z) = 10 \log \left(\frac{\hat{f}_{\mathrm{ON}}(x,z) |\mathrm{BPF}\{D_{\mathrm{ON}}(x,z;t)\}|}{\hat{f}_{\mathrm{OFF}}(x,z) |\mathrm{BPF}\{D_{\mathrm{OFF}}(x,z;t)\}|} \right) \quad (6)$$

where D_{ON} and D_{OFF} are the measurements according to (4) acquired with the magnetic field modulated ON and OFF, respectively, and $\hat{f_{\mathrm{ON}}}$ and $\hat{f_{\mathrm{OFF}}}$ are the mechanical phase filters using (5) with φ measured from D_{ON} and D_{OFF}, respectively. $S_{\mathrm{m\,m}}(x, z)$ that represents the magnetomotive signal in decibels is then displayed directly as the MM-OCT image.

III. Materials and Methods

A. Nanoparticles and Tissues

MNPs from two different sources (Sigma-Aldrich 544884-25G and Ocean NanoTech, Springdale, AR, SHP-20) with similar properties were used for the studies reported in this paper. The first type of MNPs are approximately 20–30 nm in diameter, composed of pure magnetite (Fe_3O_4), and are without any surface coating. They are easily miscible in epoxies and oil-based solvents, and were used for preparation of epoxy samples for studying MM-OCT dynamics. The second type of MNPs are monodisperse ~20 nm nanoparticles composed of a combination of magnetite/maghemite core (exact ratio proprietary) and a polymer coating with a hydrophilic COOH-terminated outer surface. These MNPs are stable in aqueous solutions (including physiological saline solutions), and were used for the tissue distribution studies.

Tissues were acquired from Wistar–Furth female inbred rats (The Jackson Laboratory, Bar Harbor, ME). The animal care and handling was performed under a protocol approved by the Institutional Animal Care and Use Committee (IACUC), University of Illinois at Urbana-Champaign. After euthanasia, the internal organs and tissues relevant for the studies were harvested and stored at −80 °C before imaging. MM-OCT imaging sequences began immediately after thawing the tissues. The tissues were immersed in a saline solution with ~5 mg/g COOH-MNPs for different time intervals at room temperature, rinsed vigorously in pure saline for less than 1 min, and imaged using MM-OCT. The time needed for each MM-OCT image acquisition was ~8 s, and the delays between each incubation period were kept as short as possible. Every effort was made to image the same tissue surface region; however, exact micrometer-scale registration between successive images was not maintained. For temperature-dependence studies, the tissues were incubated with the MNP solution in a temperature-controlled bath kept at three different temperatures.

B. Experimental Settings

A spectral-domain OCT system with a Ti:Al_2O_3 femtosecond laser (KMLabs, Inc.) producing 800 nm light with a bandwidth of 120 nm (providing l_c ~3 μm axial resolution) was used for these studies. The laser was pumped by a frequency-doubled Nd:YVO_4 laser (Coherent, Inc.) with 4.5 W of 532 nm light. The broadband light was launched into a single-mode fiber interferometer that was divided into the sample arm and a stationary reference arm. The sample beam was steered using galvanometer-mounted mirrors placed one focal length above a 30-mm achromatic imaging lens (providing Δx ~12 μm transverse resolution). A water-cooled electromagnet driven by a 250 W power supply was used to achieve a magnetic field of ~0.08 T and gradient of ~15 T/m within the sample imaging volume. The sample was scanned by the light beam through the central bore of the solenoid. The interference of the reference and sample beams was measured with a spectrometer described previously [24], composed of a grating, imaging lens, and line camera (Piranha 2, Dalsa, Inc.) with a capability of 33 kHz line acquisition rates. The spectrometer resolution was designed to provide an optical imaging depth of 2 mm.

The magnetic modulation frequency f_B varied between 50 and 100 Hz for different tissue types, based on the best response (highest A) achieved from these samples. A lower axial scan rate of 1 kHz was chosen to avoid excessive oversampling. The camera exposure time was 250 μs. The rms phase noise measured from a stationary tissue specimen at 1 kHz without transverse scanning was 0.2 rad. B-mode scans over 2.5 mm of the sample were performed with a scan velocity v of 0.625 mm/s, corresponding to a right-hand term in (1) of 104 Hz, and thus, satisfying the criterion for $f_B > 52$ Hz. Each frame consisted of 4000 pixels in width × 2048 pixels in depth, taking 4 s to acquire. Each image was acquired twice: once with the magnetic field modulated and once with the field OFF.

MM-OCT images were generated according to (6). The entire processing was carried out on a MATLAB platform. Initially, the data collected from the line camera was resampled to provide $S(\omega)$ evenly sampled in frequency ω. Median filtering of $S_{\mathrm{m\,m}}$ was performed over 23 μm × 23 μm. The BPF width was chosen to pass transverse features of $S_{\mathrm{m\,m}}$ up to a spatial frequency of 1/(32 μm). All images were downsampled by a factor of f_z/f_B along x for portability and cropped to 800 pixels in z to avoid edge effects near the bottom and top of the image.

IV. Results and Discussions

We have investigated samples in different material phases to explain the response of different biological samples to the MM-OCT system. The first curve in Fig. 1 represents a hypothetical response expected from the MM-OCT system to different material states of the samples under study. The starting point (leftmost point) is a suspension of MNPs in a medium with no elastic or viscous restoring force. Hence, any magnetomotive force on the suspended MNPs will not yield any significant MM-OCT signal from the sample. The next regime is a viscoelastic regime where the MNPs are suspended in a viscous medium.

In the viscoelastic regime, there is a viscous drag on the MNPs and some varying amount of viscoelastic forces acting on the particles. If the medium is diamagnetic by nature, this will

also oppose the magnetomotive force, but neither the media nor the MNPs will regain their initial positions after removing the magnetomotive force. Hence, we expect this region to give some amount of MM-OCT signal, but the signal would contain a variable phase lag associated with this material property regime. Because of this uncertainty, we believe that the MM-OCT signal in this material property regime is not reliably quantitative for determining the concentration of the scatterers.

The next regime is representative of an ideal Hookean system that comprises most elastic solids and biological tissues. Here, the MM-OCT signal is an accurate estimate of the nanoparticle concentration, and is also related to the elastic modulus of the material. We would measure the strongest MM-OCT signal if the sample was excited at the resonant frequency of the material corresponding to its elastic modulus. The end (right-most) portion of the curve represents an ideal hard plastic solid with high elastic modulus. No displacement of MNPs, and hence, no MM-OCT signals would be expected from samples in this high plasticity regime.

Experimentally, the starting point of this curve, shown in Fig. 1, has been verified by suspending the MNPs in a phosphate buffer solution. As postulated, we did not observe an MM-OCT signal from this medium. The second curve in Fig. 1 represents experimentally observed MM-OCT signals from epoxy samples (Embed 812 Epoxy kit, for electron microscopy studies) acquired while the epoxy was setting and hardening. The epoxy had a characteristic setting time of 12 h at a temperature of 90 °C. We used an MNP concentration of 2.5 mg/g of the epoxy mixture to prepare the sample. MM-OCT was performed at time intervals of 1 h on the samples incubated at 90 °C for 24 h. As the epoxy slowly set, the MNPs bound to the matrix and the MM-OCT signal from the sample increased, quantitatively representing the MNP concentration. As expected, the MM-OCT signal magnitude decreased as the material hardened, and decreased to <0.4 dB in 24 h, indicating that no significant MM-OCT signal was present from fully hardened epoxy, since no magnetomotion of MNPs was possible. Transmission electron microscopy (TEM) of an epoxy section showing the MNPs embedded in the epoxy matrix is shown in Fig. 2(a). We conclude from this study that a significant MM-OCT signal is observed only when the MNPs undergo their nanoscale displacements within the sample.

We performed MM-OCT on different tissues, as explained in Section III. Representative MM-OCT images of muscle and lung tissues at different time intervals are shown in Figs. 3 and 4. Fig. 5 shows a comparative plot of the total MM-OCT signal intensity (in decibels) versus time for different tissues. Each data point represents an average over ten samples, and the error bars indicate the variation in data for different experimental observations. The results show that the time for obtaining an MM-OCT signal of ~5 dB from the whole sample is around 45–60 min for muscle tissue, and around 20 min for lung tissue, whereas liver tissue becomes saturated with MNPs within 3–5 min. The rat skin remained impenetrable to the iron oxide nanoparticles even after over 8 h of immersion. This impermeability of the skin to MNPs agrees with similar studies conducted by Zvyagin *et al.* [28] on zinc oxide nanoparticle penetration in human skin. In this study, rat skin was embedded in paraffin wax with only the outer skin surface exposed to the MNP solution. The pattern of penetration of MNPs in Fig. 5 resembles a drift–diffusion process [12] that essentially depends on a

number of factors such as concentration gradient, diffusion coefficient, the viscoelastic forces in the tissue environment, various binding and affinity forces, size of particles, temperature, time of exposure, and clearance of particles. A TEM image of a muscle tissue sample incubated with MNPs for 60 min is shown in Fig. 2(b). The TEM shows the presence of MNPs dispersed within the fibrous structures of the muscle tissue. Standard protocols were used to prepare muscle tissues for TEM without any specific staining to visualize the MNP. We expect that the MNPs that are dispersed within the tissues and are bound to cellular surfaces and within interstitial spaces.

We have also investigated the temperature dependence of penetration of MNPs in muscle tissue by observing the MM-OCT signals at different time intervals for 27 °C, 37 °C, and 48 °C. The pattern of temperature dependence is plotted in Fig. 6. This shows that the rate of diffusion has a linear dependence on temperature. The result shows that the penetration and transport of MNPs is faster with increasing temperature, which corresponds to more of a temperature-dependent diffusion-like process.

We have found that the rate of transport of particles through different tissue types is directly related to their elastic modulus. Listed in Table I are the reported values of elastic moduli of various tissues from different animal models [29] and a comparison with our experimentally observed time for nanoparticle saturation in corresponding rat tissues. The penetration of MNPs is faster in tissues with lower elastic moduli. This supports the hypothesis that the MNP transport process follows a drift–diffusion model with the diffusion coefficient inversely proportional to the viscosity and/or the elastic modulus of the material.

We also observed a direct correlation between the elastic modulus of the tissue and the experimentally measured mechanical resonant frequency [30] of the magnetic field that produces the strongest MM-OCT signal (also listed in Table I). This resonant frequency is the natural frequency of oscillation of each particular type of tissue and varies strongly with the elastic modulus of the sample. As shown in Table I, stiffer samples show higher resonant frequencies. The embedded MNPs can act as dynamic nanoprobes or nanotransducers that are actuated externally using a magnetic field to evaluate the viscoelastic properties of the medium in which they are dispersed. Further studies are underway to characterize the behavior of these nanoprobes that are highly localized in viscoelastic media like phantoms and tissues. We believe that this method would find applications in real-time nondestructive analysis of tissues and various polymers.

Finally, as demonstrated in Fig. 1, our technique is not sensitive in the regime where the MNPs are unbound and rapidly diffusing through tissues. As diffusion progresses, the MNPs become bound to cellular surfaces and within the extracellular matrix due to various binding forces, and to a reduction in the concentration gradient. Hence, the MM-OCT signal from MNPs in tissue increases over time, and eventually reaches a saturation value, which is a quantitative measure of the bound MNPs in the tissue. Though the time- and temperature-dependence studies support that the process follows a drift–diffusion model, the microenvironment of the MNPs with various binding affinities and viscoelastic forces also affect MM-OCT signal.

V. Conclusion

MM-OCT provides a novel method for tracking MNPs in tissue at the microscale level. We have demonstrated imaging of diffusing MNPs in several types of *ex vivo* tissues. We were able to quantitatively estimate how the MNPs dynamically pass through tissues over time, based on the MM-OCT signal intensity observed from the tissues. We have also shown the effect of temperature on MNP transport in tissues that support a diffusion model. We have found that the rate of transport of MNPs in tissues is also directly related to the elastic properties of tissues. We conclude based on our experimental observations that transport of these MNPs in tissues follows a drift–diffusion model that depends on several parameters of the media such as viscosity, elastic modulus of tissues, temperature, concentration gradient, and binding factors. However, a comprehensive mathematical model of this entire process is complex and beyond the scope of this paper. We believe that these studies are highly relevant in knowing the actual localization and accumulation of functionalized MNPs targeted to active tumor sites. This *ex vivo* model will be helpful for understanding the dynamics of MNPs *in vivo* for future diagnostic and therapeutic oncology applications. Ongoing studies are investigating *in vivo* MM-OCT imaging of functionalized MNPs that were targeted to tumors in preclinical animal models. Currently, we are able to perform MM-OCT on anesthetized animals after exposing the tumors and internal organs to the focused OCT beam and magnetic field. Just as has been developed for internal OCT imaging, we are also developing new MM-OCT catheters and endoscopes to access internal organs for *in vivo* MM-OCT.

Although these studies are directed toward understanding the MNP dynamics in biological tissues, extensive research into other important aspects like biocompatibility, biostability, and systemic biodistribution are further needed for the complete understanding of the dynamics of these MNPs.

Acknowledgments

This work was supported in part by the National Institute of Health Roadmap Initiative under Grant 5 R21 EB005321 and Grant NIH/NIBIB 5 R01 EB005221.

The authors would like to thank Dr. A. L. Oldenburg and Dr. D. L. Marks for their technical contributions to this paper and for their insightful discussions.

References

1. Wang X, Yang L, Chen Z, Shin DM. Application of nanotechnology to cancer therapy and imaging. CA Cancer J Clin. 2008; 58:97–110. [PubMed: 18227410]
2. Loo C, Lowery A, Halas N, West J, Drezek R. Immunotargeted nanoshells for integrated cancer imaging and therapy. Nano Lett. 2005; 5:709–711. [PubMed: 15826113]
3. El-Sayed IH, Huang XH, El-Sayed MA. Surface plasmon resonance scattering and absorption of anti-EGFR antibody conjugated gold nanoparticles in cancer diagnostics: Applications in oral cancer. Nano Lett. 2005; 5:829–831. [PubMed: 15884879]
4. Thorek DLJ, Chen AK, Czupryna J, Tsourkas A. Superparamagnetic iron oxide nanoprobes for molecular imaging. Ann Biomed Eng. 2006; 34:23–38. [PubMed: 16496086]
5. Lee JH, Huh YM, Jun YW, Seo JW, Jang JT, Song HT, Kim S, Cho EJ, Yoon HG, Suh JS, Cheon J. Artificially engineered magnetic NPs for ultra-sensitive molecular imaging. Nat Med. 2007; 13:95–99. [PubMed: 17187073]

6. McCarthy JR, Weissleder R. Multifunctional magnetic nanoparticles for targeted imaging and therapy. Adv Drug Del Rev. 2008; 60:1241–1251.
7. Dobson J. Magnetic nanoparticles for drug delivery. Drug Dev Res. 2006; 67:66–60.
8. Lind K, Kresse M, Debus NP, Muller RH. A novel formulation for superparamagnetic iron oxide particles enhancing MR lymphography: Comparison of physicochemical properties and the in vivo behavior. J Drug Target. 2002; 10:221–230. [PubMed: 12075823]
9. Artemov D, Mori N, Ravi R, Bhujwalla ZM. Magnetic resonance molecular imaging of the HER-2/neu receptor. Cancer Res. 2003; 63:2723–2727. [PubMed: 12782573]
10. Bulte JWM, Kraitchman DL. Iron oxide MR contrast agents for molecular and cellular imaging. NMR Biomed. 2004; 17:484–494. [PubMed: 15526347]
11. Huang D, Swanson EA, Lin CP, Schuman JS, Stinson WG, Chang W, Hee MR, Flotte T, Gregory K, Puliafito CA, Fujimoto JG. Optical coherence tomography. Science. 1991; 254:1178–1181. [PubMed: 1957169]
12. Drexler W, Morgner U, Kartner FX, Pitris C, Boppart SA, Li XD, Ippen EP, Fujimoto JG. In vivo ultrahigh-resolution optical coherence tomography. Opt Lett. 1999; 24:1221–1223. [PubMed: 18073990]
13. Boppart SA, Oldenburg AL, Xu C, Marks DL. Optical probes and techniques for molecular contrast enhancement in coherence imaging. J Biomed Opt. 2005; 10:041208-1–041208-14.
14. Goodman TT, Chen J, Matveev K, Pun SH. Spatio-temporal modeling of nanoparticle delivery to multicellular tumor spheroids. Biotechnol Bioeng. 2008; 101:388–399. [PubMed: 18500767]
15. Graff CP, Wittrup KD. Theoretical analysis of antibody targeting of tumor spheroids: Importance of dosage for penetration and affinity for retention. Cancer Res. 2003; 63:1288–1296. [PubMed: 12649189]
16. Furlani EP, Ng KC. Analytical model of magnetic nanoparticle transport and capture in the microvasculature. Phys Rev E. 2006; 73:061919-1–061919-10.
17. Furlani EP, Ng KC. Nanoscale magnetic biotransport with application to magnetofection. Phys Rev E. 2008; 77:061914-1–061914-8.
18. Lee JH, Huh YM, Jun YW, Seo JW, Jang JT, Song HT, Kim S, Cho EJ, Yoon HG, Suh JS, Cheon J. Artificially engineered magnetic nanoparticles for ultra-sensitive molecular imaging. Nat Med. 2007; 13:95–99. [PubMed: 17187073]
19. Toublan FJJ, Boppart SA, Suslick KS. Tumor targeting by surface modified microspheres. J Amer Chem Soc. 2010; 128:3472–3473. [PubMed: 16536492]
20. Oldenburg AL, Hansen MH, Zweifel DA, Wei A, Boppart SA. Plasmon-resonant gold nanorods as low backscattering albedo contrast agents for optical coherence tomography. Opt Exp. 2006; 14:6724–6738.
21. Lee TM, Toublan FJ, Sitafalwalla S, Oldenburg AL, Suslick KS, Boppart SA. Engineered microsphere contrast agents for optical coherence tomography. Opt Lett. 2003; 28:1546–1548. [PubMed: 12956374]
22. Anker JN, Kopelman R. Magnetically modulated optical nanoprobes. Appl Phys Lett. 2003; 82:1102–1104.
23. Oldenburg AL, Gunther JR, Boppart SA. Imaging magnetically labeled cells with magnetomotive optical coherence tomography. Opt Lett. 2005; 30:747–749. [PubMed: 15832926]
24. Oldenburg AL, Toublan FJJ, Suslick KS, Wei A, Boppart SA. Magnetomotive contrast for *in vivo* optical coherence tomography. Opt Exp. 2005; 13:6597–6614.
25. Oldenburg AL, Crecea V, Rinne SA, Boppart SA. Phase-resolved magnetomotive OCT for imaging nanomolar concentrations of magnetic nanoparticles in tissues. Opt Exp. 2008; 16:11525–11539.
26. Oh J, Feldman MD, Kim J, Kang HW, Sanghi P, Milner TE. Magnetomotive detection of tissue-based macrophages by differential phase optical coherence tomography. Lasers Surg Med. 2007; 39:266–272. [PubMed: 17295337]
27. Schenck JF. Physical interactions of static magnetic fields with living tissues. Prog Biophys Mol Biol. 2005; 87:185–204. [PubMed: 15556658]

28. Zvyagin AV, Zhao X, Gierden A, Sanchez W, Ross JA, Roberts MS. Imaging of zinc oxide nanoparticle penetration in human skin in vitro and in vivo. J Biomed Opt. 2008; 13:064031-1–064031-9. [PubMed: 19123677]

29. Leventhal A, Georges P, Janmey P. Soft biological materials and their impact on cell function. Soft Matter. 2007; 3:299–306.

30. Liang X, Oldenburg AL, Crecea V, Chaney EJ, Boppart SA. Optical micro-scale mapping of dynamic biomechanical tissue properties. Opt Exp. 2008; 16:11052–11065.

Biographies

Renu John was born in Kerala, India, in 1976. He received the B.Sc. degree from Mahathma Gandhi University, Kottayam, Kerala, in 1996, the M.Sc. degree from Cochin University of Science and Technology, Kochi, Kerala, in 1999, and the Ph.D. degree from Indian Institute of Technology Delhi, Delhi, India, in 2006, all in Physics.

He was a Postdoctoral Research Associate in Duke University, Durham, NC, from 2006 to 2008. He is currently a Research Associate in Beckman Institute for Advanced Science and Technology, University of Illinois at Urbana-Champaign, Urbana-Champaign. He was engaged in secure holographic memories and the applications of phase-based data storage in content search. His current research interests include the development of novel molecular contrast imaging techniques and associated nanoparticles for use with optical coherence tomography. He has authored or coauthored 11 contributed publications and has presented papers in more than 15 international conferences.

Dr. John is a member of the Optical Society of America, and the Laser and Spectroscopy Society of India.

Eric J. Chaney was born in Mount Vernon, IL, in 1970. He received the B.S. degree in biology from the University of Evansville, Evansville, IN, in 1992.

From 1993 to 1997, he was a Research Assistant in Indiana University School of Medicine, Indiana State University, Terre Haute. From 1997 to 2000, he was a Transmission Electron Microscope Technician at the University of Illinois at Urbana-Champaign. He currently is a

Research Specialist in molecular biology at the Beckman Institute for Advanced Science and Technology at the University of Illinois at Urbana-Champaign.

Stephen A. Boppart (S'90–M'90–SM'06) was born in Harvard, IL, in 1968. He received the B.S. degree in electrical and bioengineering, the M.S. degree in electrical engineering, and the Residency Training in internal medicine from the University of Illinois at Urbana-Champaign, Urbana-Champaign, in 1990, 1991, and 2005, respectively, the Ph.D. degree in electrical and medical engineering from Massachusetts Institute of Technology, Cambridge, in 1998, and the M.D. degree from Harvard Medical School, Boston, MA, in 2000.

He was a Research Scientist in the Air Force Laser Laboratory, Brooks Air Force Base, San Antonio, TX, where he was engaged in research on developing national (American National Standards Institute) and Air Force laser safety standards. Since 2000, he has been with the University of Illinois at Urbana-Champaign, where he is currently a Professor of electrical and computer engineering, bioengineering, and medicine, and the Head of the Biophotonics Imaging Laboratory, Beckman Institute for Advanced Science and Technology. He is also the Leader of a campus-wide imaging initiative. He has authored or coauthored more than 165 invited and contributed publications, and over 400 invited and contributed presentations, and holds more than 25 patents filed or pending. His current research interests include the development of novel optical imaging technologies for biological and medical applications, with particular emphasis on translating these to clinical applications in cancer detection and diagnosis.

Prof. Boppart is a Fellow of the Optical Society of America and the International Society for Optical Engineering, and a member of the Society for Molecular Imaging, the Academy of Molecular Imaging, the American Association for the Advancement of Science, the American Association for Cancer Research, and the American Medical Association. He was named as one of the Top 100 Innovators in the World by the Technology Review Magazine for his research in medical technology in 2002. He received the IEEE Engineering in Medicine and Biology Society Early Career Achievement Award in 2005.

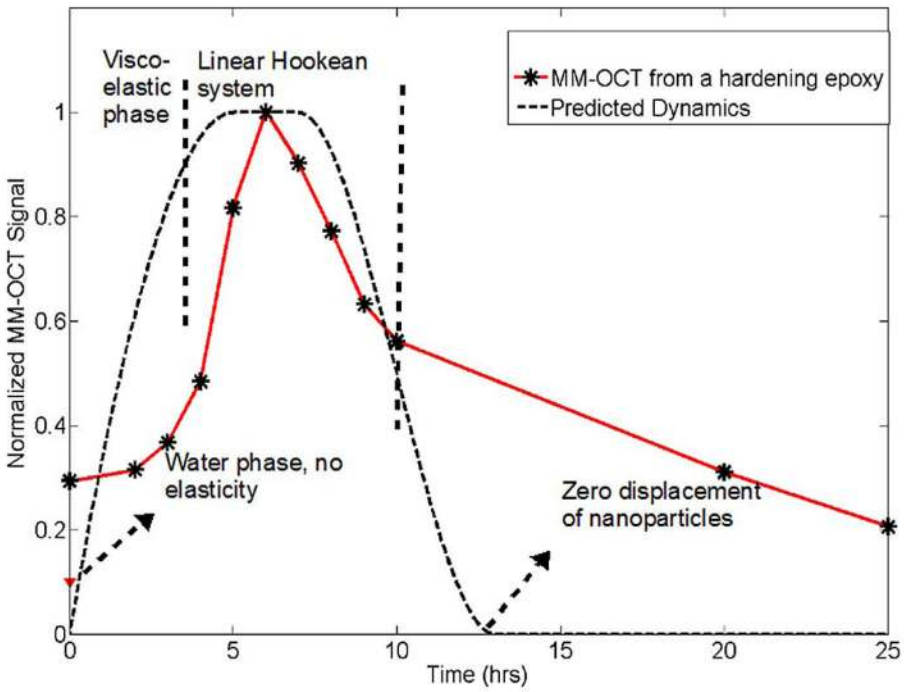

Fig. 1.

MM-OCT signal intensity as a function of time. A predicted response curve is compared with experimental data from a hardening epoxy sample and from MNPs suspended in phosphate buffer.

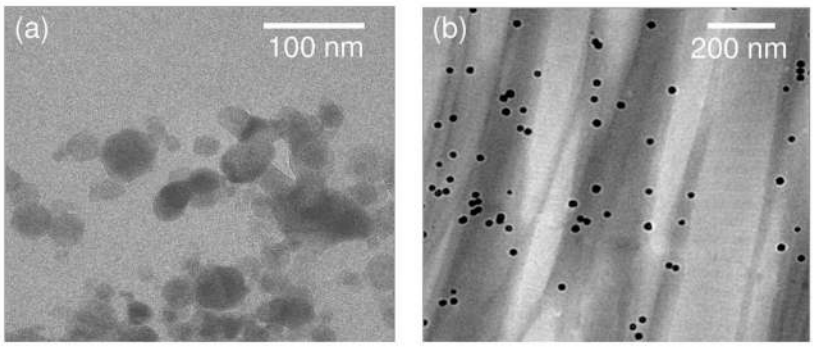

Fig. 2.

TEM images of (a) iron oxide nanoparticles (Sigma Aldrich) embedded in hardened epoxy and (b) iron oxide nanoparticles (Ocean Nanotech) diffused into muscle tissue. Note the different size scales between images, and the appearance of the polymer coating on the MNPs shown in (b).

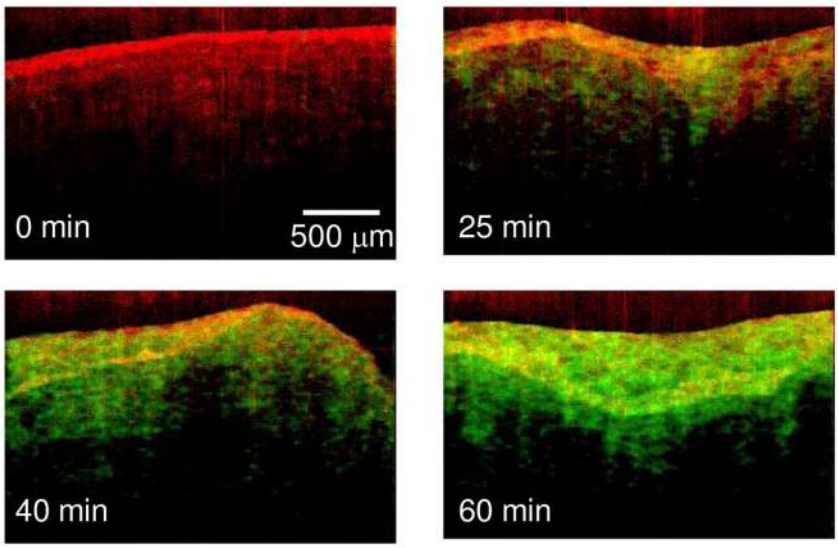

Fig. 3.

MM-OCT images of muscle tissue acquired at intervals of 0, 25, 40, and 60 min after immersion in the MNP solution. The MM-OCT signal is shown, superimposed over the structural OCT signal. (Appear in color online with green channel representing MM-OCT signal and red channel representing OCT signal.)

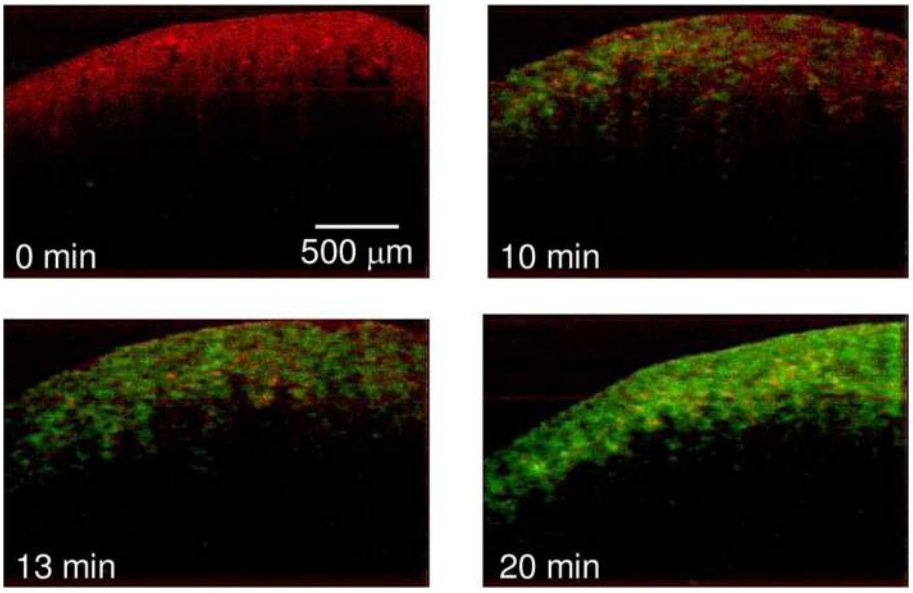

Fig. 4.

MM-OCT images of lung tissue acquired at intervals of 0, 10, 13, and 20 min after immersion in the MNP solution. The MM-OCT signal is shown, superimposed over the structural OCT signal. (Appear in color online with green channel representing MM-OCT signal and red channel representing OCT signal.)

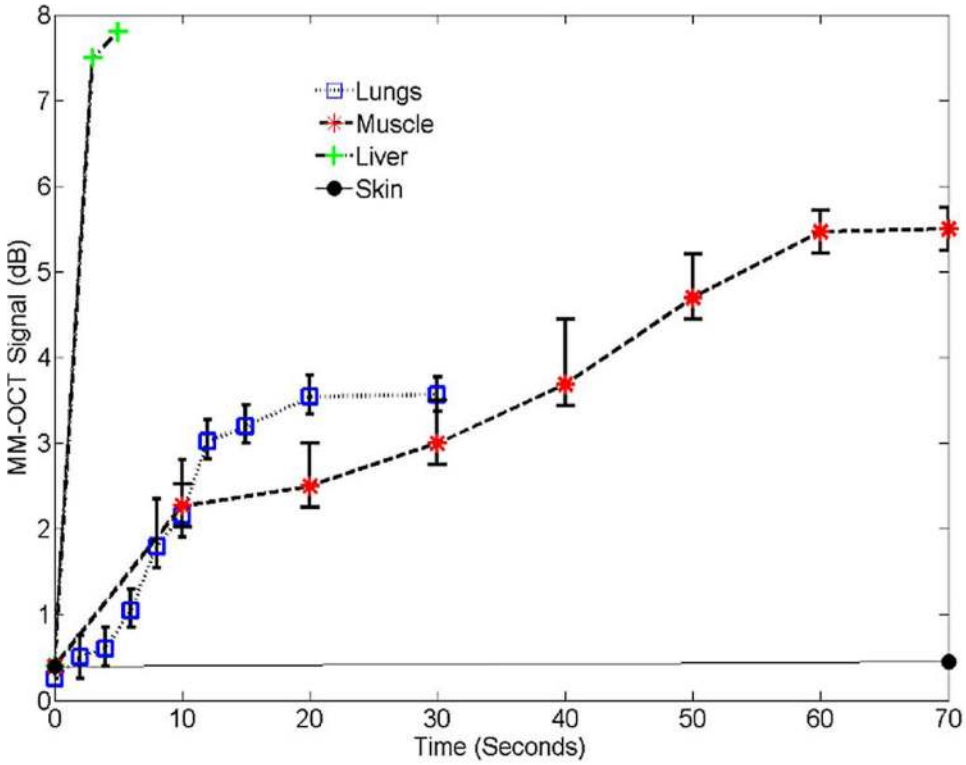

Fig. 5.
MM-OCT signal intensity as a function of time for different tissues.

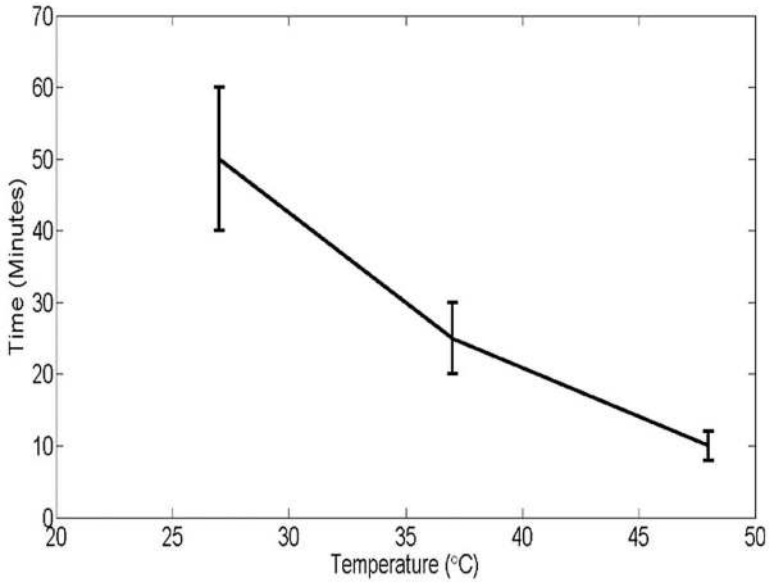

Fig. 6.

Time versus temperature plot for MNP transport through muscle tissue. The vertical axis denotes the time taken for obtaining a saturated MM-OCT signal and horizontal axis shows the temperature in degree Celsius.

TABLE I

Comparison of Observed MNP Transport Time With Reported Values of Elastic Modulus for Different Tissue Types Along With Measured MM-OCT Resonant Frequency

Tissue	Elastic modulus [29]	Penetration time in rat tissue	Resonant frequency
Fat (Human)	17 Pa	<1 min	45 Hz
Liver (Human)	640 Pa	5 min	56 Hz
Lungs (G. Pig)	5–6 kPa	20 min	90 Hz
Muscle (Rat)	12–100 kPa	60 min	100 Hz
Kidney (Swine)	25 kPa	------	100 Hz